nature nanotechnology

ARTICLES

PUBLISHED ONLINE: 7 SEPTEMBER 2015 | DOI: 10.1038/NNANO.2015.194

A phosphorene–graphene hybrid material as a high-capacity anode for sodium-ion batteries

Jie Sun[1†], Hyun-Wook Lee[1†], Mauro Pasta[1], Hongtao Yuan[2,3], Guangyuan Zheng[4], Yongming Sun[1], Yuzhang Li[1] and Yi Cui[1,3*]

Sodium-ion batteries have recently attracted significant attention as an alternative to lithium-ion batteries because sodium sources do not present the geopolitical issues that lithium sources might. Although recent reports on cathode materials for sodium-ion batteries have demonstrated performances comparable to their lithium-ion counterparts, the major scientific challenge for a competitive sodium-ion battery technology is to develop viable anode materials. Here we show that a hybrid material made out of a few phosphorene layers sandwiched between graphene layers shows a specific capacity of 2,440 mA h g^{-1} (calculated using the mass of phosphorus only) at a current density of 0.05 A g^{-1} and an 83% capacity retention after 100 cycles while operating between 0 and 1.5 V. Using *in situ* transmission electron microscopy and *ex situ* X-ray diffraction techniques, we explain the large capacity of our anode through a dual mechanism of intercalation of sodium ions along the *x* axis of the phosphorene layers followed by the formation of a Na_3P alloy. The presence of graphene layers in the hybrid material works as a mechanical backbone and an electrical highway, ensuring that a suitable elastic buffer space accommodates the anisotropic expansion of phosphorene layers along the *y* and *z* axial directions for stable cycling operation.

Sodium-ion batteries have received a great deal of attention lately as an attractive alternative to lithium-ion batteries, because sodium resources are virtually inexhaustible and are ubiquitous around the world[1]. Recent studies on sodium-ion battery cathode materials have reported performances comparable to their lithium-ion battery counterparts[2–4]. The major scientific challenge for sodium-ion batteries therefore resides in developing a new anode material with a high specific capacity and an appropriately low redox potential. Adapting lithium-ion battery anode materials to sodium-ion batteries has so far been unsuccessful. Metallic sodium is not a suitable material because of dendrite formation and its low melting point (98 °C)[5], and graphite is electrochemically inactive due to the large size of the sodium ions (2.04 Å) compared with the channel size of the graphene layers (1.86 Å)[6]. It has recently been shown that the graphene interlayer distance could be increased to 4.3 Å and the sodium ions inserted reversibly, with promising capacity retention[7]. However, only a modest specific capacity of 284 mA h g^{-1}, insufficient for applications, was measured. Other carbon anodes, for example composed of hard carbon or amorphous carbon, show specific capacities of less than 300 mA h g^{-1} [5]. Silicon, despite the theoretical existence of Na–Si alloys, is also electrochemically inactive[8]. Other group IV elements such as germanium ($Na_{15}Ge_4$, 369 mA h g^{-1})[9,10], tin ($Na_{15}Sn_4$, 847 mA h g^{-1})[11,12] or lead ($Na_{15}Pb_4$, 485 mA h g^{-1})[13], and group V elements such as antimony (Na_3Sb, 660 mA h g^{-1})[14], have been suggested as promising anode candidates, but they exhibit specific capacities below 1,000 mA h g^{-1} and limited cycle life (Supplementary Table 1).

Phosphorus reacts electrochemically with both lithium and sodium to form Li_3P and Na_3P at an attractive potential for an anode material and with a high theoretical specific capacity of 2,596 mA h g^{-1}, which significantly exceeds that of any other sodium-ion battery anode presently available. Phosphorus exists in three main allotropes: white, red and black[15]. White phosphorus consists of tetrahedral P_4 molecules. It is highly reactive and toxic and therefore unsuitable as a battery material[16]. Amorphous red phosphorus has been investigated previously as an anode material for both lithium-ion[17–19] and sodium-ion batteries[20–23], but its poor electrical conductivity results in a modest cycle life and rate performance. Orthorhombic black phosphorus with its layered crystal structure is the most thermodynamically stable allotrope[24,25]. In terms of appearance, properties and structure, black phosphorus closely resembles graphite: it is black and flaky, a good conductor of electricity (~300 S m^{-1}), and it is made of puckered sheets of covalently bonded phosphorus atoms[24,25]. Compared with graphite, black phosphorus has a larger interlayer channel size (3.08 versus 1.86 Å), meaning that both lithium (1.52 Å) and sodium (2.04 Å) ions can be stored between the phosphorene layers. Although black phosphorus has been reported previously in the literature as an anode for lithium-ion batteries[26–29], its poor cycling performance for sodium-ion batteries needs to be improved[30]. It is therefore important to investigate the sodiation mechanism in order to optimize the performance of black phosphorus for use in sodium-ion batteries.

In this Article, we investigate the sodiation mechanism of black phosphorus using *in situ* transmission electron microscopy (TEM) and *ex situ* X-ray diffraction (XRD) techniques. A two-step sodiation mechanism of intercalation and alloying is demonstrated. A large anisotropic volumetric expansion along the *y* and *z* axial directions is observed during the alloy reaction, which leads to a significant capacity decay with cycling. To achieve both high capacity and stable cyclability, we have specifically designed a nanostructured phosphorene–graphene hybrid with a few phosphorene layers sandwiched between graphene layers. The advantages of our structure design are threefold: (1) the graphene layers

[1]Department of Materials Science and Engineering, Stanford University, Stanford, California 94305, USA. [2]Geballe Laboratory for Advanced Materials, Stanford University, Stanford, California 94305, USA. [3]Stanford Institute for Materials and Energy Sciences, SLAC National Accelerator Laboratory, 2575 Sand Hill Road, Menlo Park, California 94025, USA. [4]Department of Chemical Engineering, Stanford University, Stanford, California 94305, USA. †These authors contributed equally to this work. *e-mail: yicui@stanford.edu

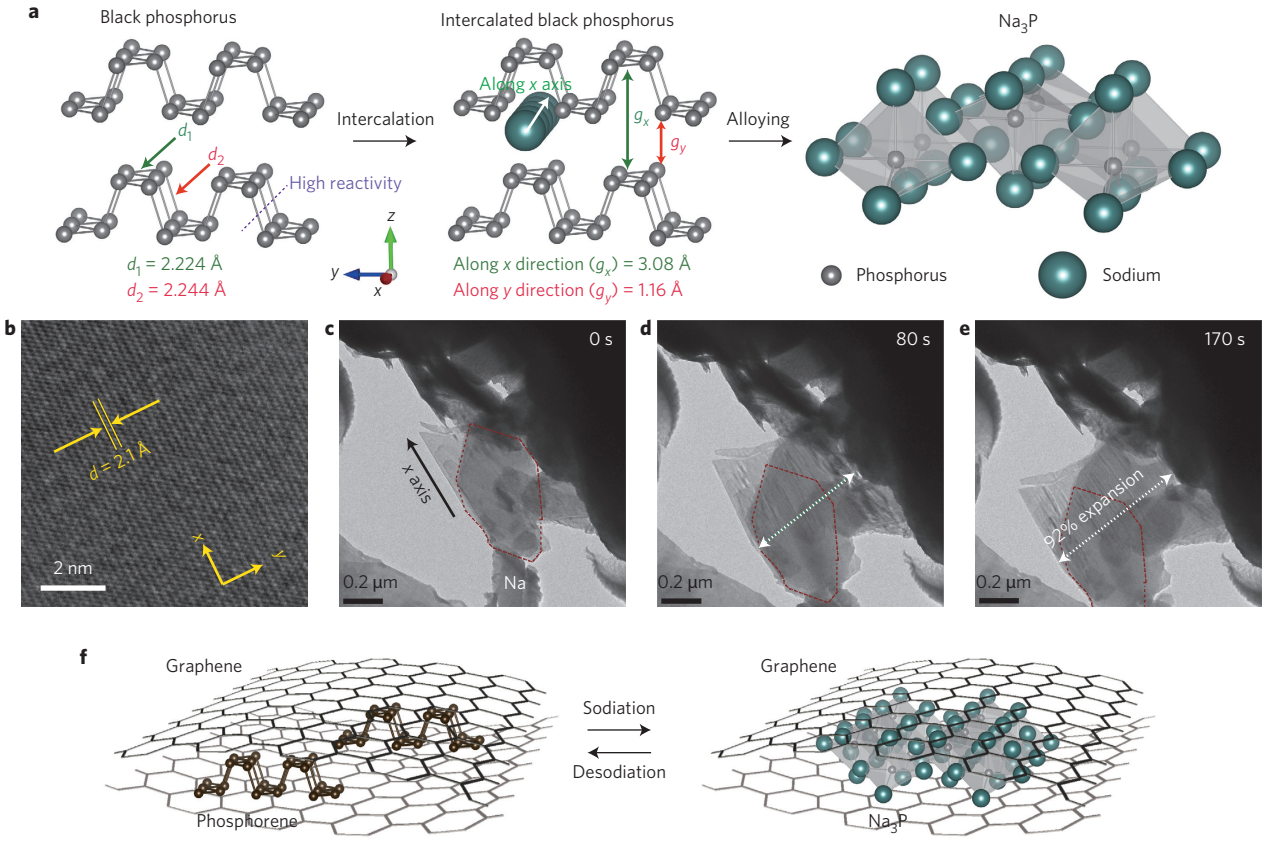

Figure 1 | Mechanism of sodiation in black phosphorus. a, Schematics of black phosphorus before sodiation, with the first step of sodium-ion intercalation, and the second step of alloy reaction to form Na_3P. **b**, High-resolution and bright-field TEM image of black phosphorus before sodiation. **c**–**e**, Time-lapse TEM images of sodiation in black phosphorus. Sodium ions transport along the *x*-axis channel, causing a volume expansion along the *y*-axis direction. **f**, Structural evolution of the sandwiched phosphorene–graphene structure during sodiation.

provide an elastic buffer layer to accommodate the anisotropic volumetric expansion during the sodiation process; (2) the phosphorene layers offer a short diffusion distance for sodium ions; (3) the graphene layers function as an electrical highway, so the hybrid material is electrochemically active.

Mechanisms of sodiation in black phosphorus

The storage of sodium ions in black phosphorus proceeds according to two different reaction mechanisms of intercalation and alloying, as shown in Fig. 1a. Sodium ions are first inserted between the phosphorene layers (intercalation), along the *x*-axis-oriented channels. Indeed, only the channels along the *x* axis are wide enough (3.08 Å) to allow the diffusion of sodium ions (2.04 Å), the channels along the *y* axis being too small at 1.16 Å. An *ex situ* XRD diffractogram of black phosphorus before sodiation (Supplementary Fig. 2) show two characteristic diffraction peaks at 16.9° ($d = 5.24$ Å) and 34.2° ($d = 2.62$ Å), attributed to the diffraction of the (002) and (004) crystal planes, respectively. These two peaks shift towards a lower angle with the sodiation of black phosphorus, indicating that the distance between the phosphorene layers along the *z* axis has increased and revealing the intercalation of sodium ions. The two XRD peaks are clearly visible until the potential reaches 0.54 V (Supplementary Fig. 2b,c), clearly showing that the layered structure is preserved upon cycling. This mechanism is similar to the intercalation process occurring in graphite upon lithiation, generating the LiC_6 phase[31]. The intercalation does not significantly alter the host structure, thus guaranteeing high reversibility upon cycling in the 0.54–1.5 V region (Supplementary Fig. 3a). Nonetheless, the specific capacity is limited to the impractical value of 150 mA h g^{-1}, that is, $Na_{0.17}P$.

Further sodiation below 0.54 V results in the formation of Na_xP species (alloy reaction), with the consequent disappearance of the characteristic black phosphorus XRD peaks (Supplementary Fig. 2). Diffraction peaks of the intermediate Na_xP phases were difficult to identify due to domain size, poor crystallinity and the Kapton tape background used to encapsulate the air-sensitive electrodes. However, when the potential reaches 0.1 V and the alloy reaction is close to completion, the distinctive (110) and (103) peaks of the Na_3P phase are clearly recognized at 36.0° ($d = 2.49$ Å) and 37.0° ($d = 2.42$ Å) (Supplementary Fig. 2a). The alloying mechanism is therefore primarily responsible for the outstanding specific capacity of black phosphorus (Supplementary Fig. 3c). However, this mechanism also results in a large volume expansion of ~500%, which causes mechanical and structural fracturing (Supplementary Fig. 4), leading to significant capacity loss upon cycling (Supplementary Fig. 3d). These challenges are similar to those with other high-capacity materials such as silicon[32,33] and sulphur[34].

It is therefore necessary to understand the nature of the stress evolution in black phosphorus in order to efficiently tackle these problems by developing innovative materials structures. Figure 1b,c presents TEM images of a black phosphorus particle before *in situ* sodiation. The longer, clean-cut edge of the particle is aligned along the *x*-axis direction. In fact, cutting along the *x* axis requires only four P–P bonds to be broken, which are longer (2.244 Å) and therefore weaker (purple dashed line in Figs 1a and 2d). It would be impossible to obtain such a clean-cut edge along the *y*-axis direction given that the shorter (2.224 Å) P–P bond would still hold the phosphorene layers together. Moreover, we observed many nanobelt-like objects among the general nanosheet structures (Supplementary Figs 6 and 7). All the nanobelts are also clean-cut

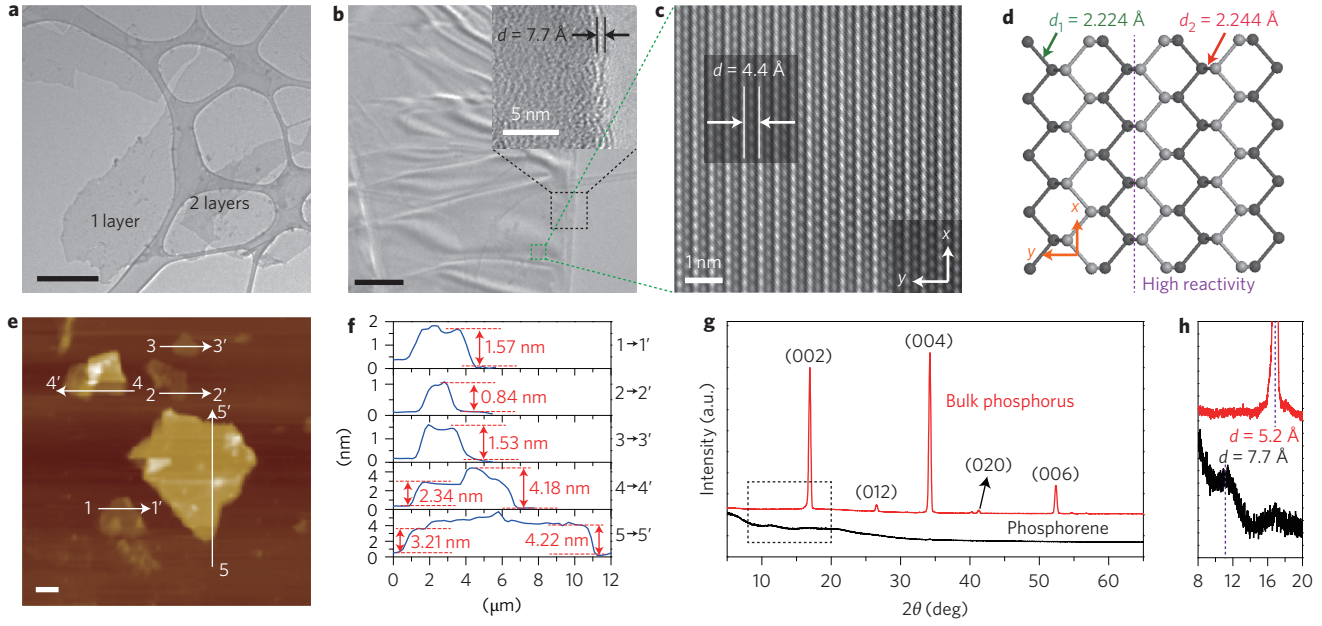

Figure 2 | Evidence of monolayer and few-layer phosphorene. a, TEM image of monolayer phosphorene. Scale bar, 2 μm. **b**, TEM image of trilayer phosphorene nanobelt showing the long side. Scale bar, 200 nm. Inset: HRTEM image of the edge. **c**, HRTEM image of selected area of **b** with measured lattice spacing. **d**, Schematic of square phosphorene (top view) with labelled bond lengths. **e**, AFM image of monolayer and few-layer phosphorene. Scale bar, 2 μm. **f**, Measured thickness of the phosphorene in **e**. **g**, XRD pattern of black phosphorus and phosphorene. **h**, Amplification of XRD pattern of black phosphorus and phosphorene in the low-angle range (dashed rectangle in **g**).

along their longer sides (Fig. 2b), and always aligned along the *x* axis, according to the high-resolution (HR) TEM image in Fig. 2c.

The potentiostatic sodiation of the black phosphorus particle (Fig. 1c) occurred as it was separated from the sodium metal electrode by a native sodium oxide layer acting as a solid electrolyte (Supplementary Section 1.3, '*In situ* TEM'). Figure 1d,e shows the black phosphorus particle after 80 and 170 s (Supplementary Movie 1), respectively. A 92% expansion along the *y* axis was observed, while the particle dimension along the *x* axis remained nearly unchanged. The anisotropic expansion along the *y* axis is the result of easier sodium ion diffusion along the *x* axis and the weaker P–P bonding along the *x* axis. The full sodiation in black phosphorus forming Na_3P has a theoretical volume expansion of ~500% and the *x* and *y* axis expansions have been measured to be 0 and 92%, respectively. From this, we infer that a significant expansion (~160%) along the *z* axis is also taking place. Therefore, minimizing the width and the thickness of the black phosphorus layers would help reduce the stress built up along the critical *y* and *z* axial directions. In this sense, an electrode made of monolayer black phosphorus (phosphorene)[35–38] would be ideal. In broad terms, few-layer (<10 layers) black phosphorus can be defined as phosphorene, much the same as graphene[39,40]. Moreover, sandwiching small phosphorene layers between large graphene sheets (Fig. 1f) could lead to the following additional benefits: (1) the ultrathin phosphorene minimizes the diffusion distance of both sodium ions and electrons, resulting in an enhanced rate performance; (2) the graphene layers can facilitate the transport of electrons generated in the phosphorene redox reaction to the current collector; (3) the space between phosphorene nanosheets provides an elastic buffer space to accommodate anisotropic expansion.

Fabrication of phosphorene–graphene hybrids

Few-layer phosphorene nanosheets were exfoliated using a technique similar to a previously reported method[41,42] that is versatile and solution-based, making it relatively scalable, and with yields approaching 17 wt% (see Methods). The as-synthesized few-layer phosphorene nanosheets were imaged by TEM (Fig. 2a,b) and atomic force microscopy (AFM) (Fig. 2e,f). Their thicknesses ranged between 0.84 and 4.22 nm, equivalent to one to five phosphorene layers (rarely did the thickness exceed five layers). The width of each nanosheet ranged between 700 nm and 10 μm. The HRTEM image in the inset to Fig. 2b shows a nanosheet made of three phosphorene layers with a [002] lattice spacing of 7.7 Å, which is larger than the 5.2 Å of black phosphorus, as confirmed by an XRD diffractogram (Fig. 2g,h). Thus, the *x* and *y* channel sizes increase to 3.7 and 5.6 Å, respectively, opening the *y* channel to sodium ion (2.04 Å) diffusion.

The structural differences between black phosphorus (>10 layers) and the phosphorene nanosheets (1–5 layers) were further investigated by Raman spectroscopy (Supplementary Fig. 5a). Atomic displacements of Raman active modes corresponding to one out-of-plane mode (A_g^1) and two in-plane modes (A_g^2 and B_{2g})[43–45] are shown in Supplementary Fig. 5b. We observed A_g^1, A_g^2 and B_{2g} modes in both black phosphorus and phosphorene samples, with the ratios A_g^2/A_g^1 and A_g^2/B_{2g} increasing as the number of phosphorene layers decreased. For mono- and bilayer phosphorene, the A_g^2 mode shifted from 467.7 cm^{-1} (3–5 layers) to 469.6 and 468.8 cm^{-1}, respectively. Black phosphorus is a unique anisotropic material with the lattice parameters in different directions exhibiting different sensitivities to external impacts, so the in-plane mode A_g^2 vibration stiffens with a decrease in thickness, while the B_{2g} and A_g^1 modes remain almost unchanged[46].

The phosphorene–graphene sandwich structure was achieved simply by mixing *N*-methyl-2-pyrrolidone (NMP) dispersions of phosphorene and graphene (Fig. 3a), followed by self-assembly after NMP evaporation in an argon-filled glove box (see Methods). TEM images with energy-dispersive X-ray spectroscopy (EDS) mapping (Supplementary Fig. 8) show phosphorene nanosheets uniformly distributed and sandwiched between the wider graphene nanosheets. The HRTEM image of the cross-section reported in Fig. 3c shows a thickness of 2–5 nm, with alternating phosphorene and graphene layers. Raman spectroscopy

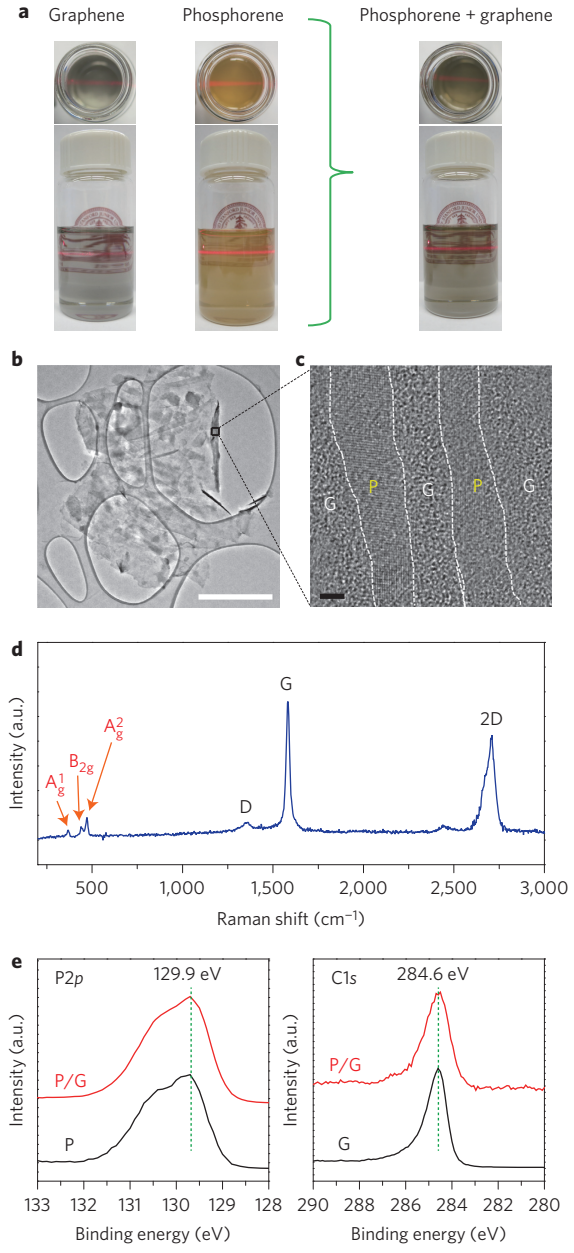

Figure 3 | Physical characterization of the phosphorene–graphene hybrid structure. a, Digital photographs of NMP dispersions of graphene (3 μg ml^{-1}), phosphorene (17 μg ml^{-1}) and a mixture prepared by mixing the dispersions of graphene and phosphorene at a volume ratio of 6:1, corresponding to a carbon–phosphorus molar ratio of 2.78:1. Red light beams were incident from the side to demonstrate the Tyndall effect. **b**, TEM image of the phosphorene–graphene hybrid. Scale bar, 2 μm. **c**, HRTEM image of the cross-section of the phosphorene–graphene hybrid (the turned-up right edge in **b**). Scale bar, 2 nm. **d**, Raman spectra of phosphorene–graphene hybrid with the modes of both phosphorene (A_g^1, A_g^2 and B_{2g}) and graphene (G and 2D). **e**, XPS analysis of the C1*s* and P2*p* peaks from graphene, phosphorene and phosphorene–graphene. Graphene, phosphorene and the phosphorene–graphene hybrid are labelled G, P and P/G, respectively, in **c** and **e**.

(Fig. 3d) shows the A_g^1, A_g^2 and B_{2g} modes of phosphorene, as well as the distinct G and 2D modes characteristic of graphene[39,40]. The position of the A_g^2 peak and the intensity of the ratios A_g^2/A_g^1 and A_g^2/B_{2g} correspond to nanosheets made of five phosphorene layers or less[46]. Phosphorene–phosphorene self-assembly is hindered by the poor affinity between the phosphorene layers, due to their buckled structure. The X-ray photoemission spectroscopy (XPS) peaks at the P2*p* and C1*s* edges are not significantly affected by the self-assembly process (Fig. 3e). This clearly indicates that no chemical reaction occurs during the synthesis and that the structure is held together by van der Waals forces.

Electrochemical testing of phosphorene–graphene hybrids

The carbon–phosphorus (C/P) mole ratio in the hybrid structure is an important parameter that requires further optimization. In fact, some buffer space between different phosphorene nanoplates should be reserved for the *y*-axis directional expansion of phosphorene upon sodiation. The C/P ratio was calculated based on the area ratio of monolayer graphene and phosphorene (Supplementary Section 2.4, 'Phosphorene/graphene hybrid'). Considering that the real nanosheets are made of more than one monolayer, we experimentally investigated the cycling performance of the phosphorene–graphene hybrids with various C/P ratios. The galvanostatic cycling at 0.02 C (0.05 A g^{-1}) (Fig. 4a) shows that samples prepared using C/P ratios of 2.78:1 and 3.46:1, respectively, exhibit a similar capacity retention after 100 cycles. A lower C/P ratio is obviously beneficial in terms of specific capacity, given that graphene is electrochemically inactive for sodiation. Therefore, the following electrochemical characterization was carried out on the optimized 2.78:1 C/P ratio, corresponding to 48.3% of phosphorus by mass.

The electrochemical performance of the phosphorene–graphene sandwiched structure was tested in a two-electrode arrangement, in the 1.5–0.02 V potential range and at a 0.02 C rate (50 mA g^{-1}) (Fig. 4b). The first discharge cycle shows three distinct electrochemical processes. The first region between 1.2 and 0.6 V corresponds to the irreversible formation of the solid-electrolyte interphase (SEI) layer (Supplementary Fig. 9), which is responsible for the modest first-cycle Coulombic efficiency of ~80%. Two additional plateaux are located at 0.58 and 0.2 V, corresponding to the intercalation and alloy reaction, respectively. In subsequent cycles the 0.58 V plateau disappears, as the phosphorene layers do not survive the intercalation reaction. Although the phosphorene layer transformed to an amorphous structure (Supplementary Fig. 4c) after one cycle, it was still confined between graphene interlayers, resulting in a stable sandwiched structure (Supplementary Fig. 11). A shorter plateau can be seen at ~0.4 V, which may be due to the nucleation of a Na_xP phase. The first cycle reversible capacity was 2,440 mA h g^{-1} based on the mass of the phosphorus. The contribution of graphene to the reversible capacity is negligible (~40 mA h g^{-1}, Supplementary Fig. 13). The theoretical specific capacity of phosphorus is 2,596 mA h g^{-1} and the phosphorene–graphene hybrid delivered 94% of the theoretical capacity (equivalent to $Na_{2.82}P$). To test the efficacy of our sandwich design, the electrochemical performance of an electrode prepared by mixing black phosphorus and graphene with the same C/P ratio of 2.78:1 was also measured, and a low reversible capacity of ~700 mA h g^{-1} was observed (Supplementary Fig. 3c).

Due to its enhanced electrical conductivity, the phosphorene–graphene sandwiched structure showed very good cycling capability (Fig. 4c). A reversible capacity of 2,440 mA h g^{-1} was obtained at 0.02 C (50 mA g^{-1}). When the current rate was increased to 0.08 C (0.2 A g^{-1}), it could still deliver a reversible capacity of 2,320 mA h g^{-1}. Even at the very high rates of 3 C (8 A g^{-1}), 4.6 C (12 A g^{-1}), 7.7 C (20 A g^{-1}) and 10 C (26 A g^{-1}), the electrode retained a specific capacity of 1,450 mA h g^{-1} (59.4%), 1,200 mA h g^{-1} (49.2%), 915 mA h g^{-1} (37.5%) and 645 mA h g^{-1} (26.4%), respectively. Moreover, the phosphorene–graphene sandwiched structure shows good capacity retention upon cycling (Fig. 4d). After 100 cycles at a rate of 0.02 C (50 mA g^{-1}), a specific capacity of 2,080 mA h g^{-1} was still available, corresponding to an 85% capacity retention (0.16% decay per cycle). At relatively fast rates of 3 C (8 A g^{-1})

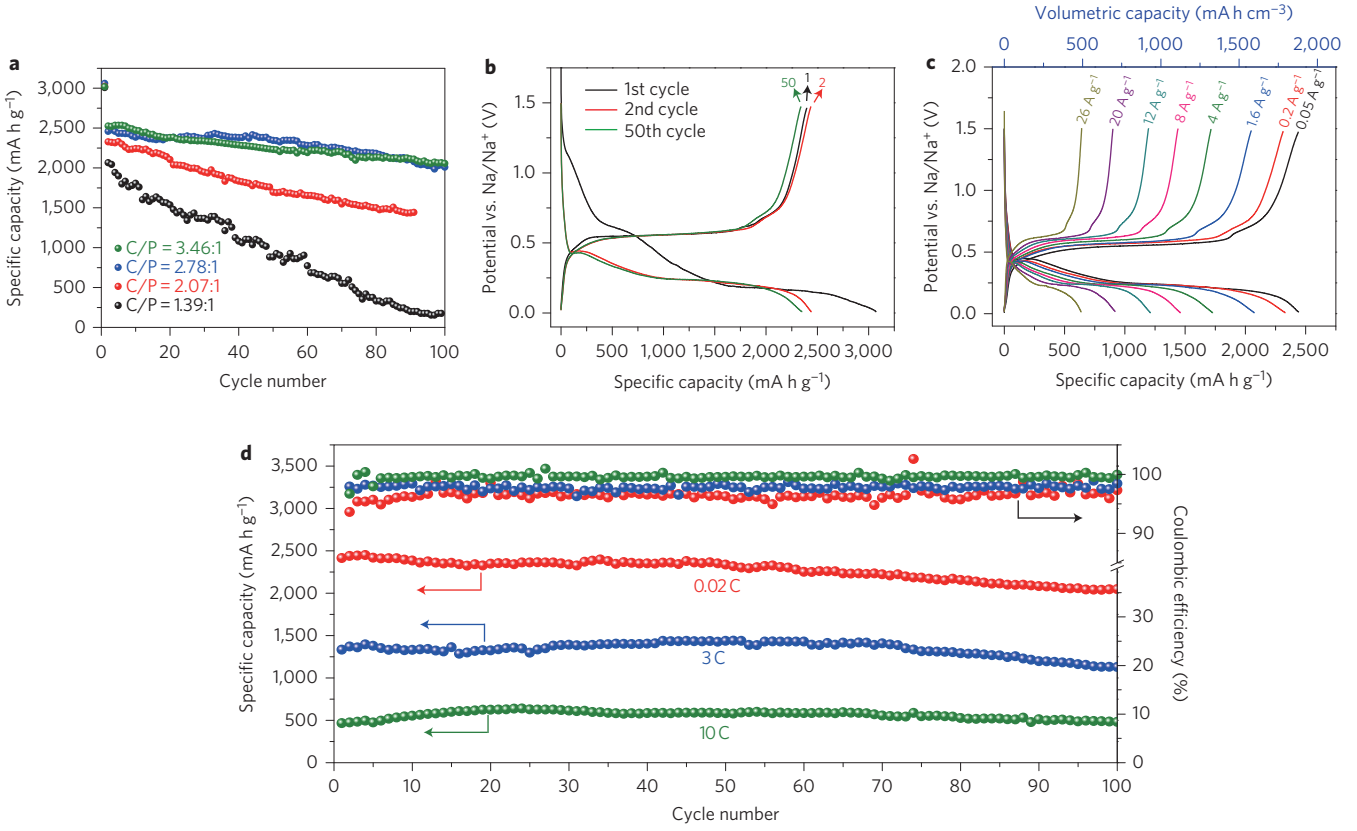

Figure 4 | Electrochemical characterization of the phosphorene–graphene anode for sodium-ion batteries. All specific capacities of the phosphorene–graphene anode are based on the mass of the phosphorene, because the contribution of graphene to the reversible capacity is negligible. **a**, Reversible desodiation capacities for the first 100 galvanostatic cycles of various phosphorene–graphene electrodes with different carbon–phosphorus mole ratios (C/P) of 1.39, 2.07, 2.78 and 3.46, between 0.02 and 1.5 V at a current density of 0.05 A g^{-1}. **b**, Galvanostatic discharge–charge curves of the phosphorene–graphene (48.3 wt% P) anode plotted for the first, second and 50th cycles. **c**, Volumetric and mass capacities at different current densities (from 0.05 to 26 A g^{-1}). **d**, Reversible desodiation capacity and Coulombic efficiency for the first 100 galvanostatic cycles of the phosphorene/graphene (48.3 wt% P) anode tested under different currents.

and 10 C (26 A g^{-1}), the capacity retentions were 84 and 77%, respectively, after 100 cycles. SEI breakdown and reformation usually results in a poor Coulombic efficiency, an indicator of the reversibility of the electrode reaction. At the relatively fast rates of 3 C (8 A g^{-1}) and 10 C (26 A g^{-1}), the average Coulombic efficiencies were 97.6 and 99.3%, respectively, in the first 100 cycles. With an increase of mass loading from 0.5 to 2 mg cm^{-2}, despite the fact that specific capacities decrease by 5–12% at various C rates, the phosphorene–graphene structure still exhibited a high capacity retention of 88% after 70 cycles at a rate of 0.7 C (1.8 A g^{-1}) (Supplementary Fig. 12), an indication of the stability of the hybrid material.

Conclusions

We have reported a sandwiched phosphorene–graphene hybrid material that shows high specific capacity, rate capability and cycle life as an anode material in sodium-ion batteries. The graphene layers provide an elastic buffer layer to accommodate the expansion of phosphorene layers along the *y* and *z* axial directions during the alloy reaction to Na_3P. The phosphorene nanosheets, with increased interlayer distance, offer a short and effective diffusion distance for sodium ions. Moreover, the graphene enhances both the electrical conductivity of the material and provides a preferential pathway to the electrons generated by the redox reaction of phosphorene. The facile synthesis and superior electrochemical properties of our sandwiched phosphorene–graphene hybrid could render it a suitable anode material for sodium-ion batteries.

Methods

Methods and any associated references are available in the online version of the paper.

Received 30 October 2014; accepted 27 July 2015; published online 7 September 2015

References

1. Slater, M. D., Kim, D., Lee, E. & Johnson, C. S. Sodium-ion batteries. *Adv. Funct. Mater.* **23,** 947–958 (2013).
2. Barpanda, P., Oyama, G., Nishimura, S.-I., Chung, S.-C. & Yamada, A. A 3.8-V earth-abundant sodium battery electrode. *Nature Commun.* **5,** 4358 (2014).
3. Ellis, B. L., Makahnouk, W. R. M., Makimura, Y., Toghill, K. & Nazar, L. F. A multifunctional 3.5 V iron-based phosphate cathode for rechargeable batteries. *Nature Mater.* **6,** 749–753 (2007).
4. Lee, H.-W. *et al.* Manganese hexacyanomanganate open framework as a high-capacity positive electrode material for sodium-ion batteries. *Nature Commun.* **5,** 5280 (2014).
5. Palomares, V. *et al.* Na-ion batteries, recent advances and present challenges to become low cost energy storage systems. *Energy Environ. Sci.* **5,** 5884–5901 (2012).
6. Komaba, S. *et al.* Electrochemical Na insertion and solid electrolyte interphase for hard-carbon electrodes and application to Na-ion batteries. *Adv. Funct. Mater.* **21,** 3859–3867 (2011).
7. Cao, Y. L. *et al.* Sodium ion insertion in hollow carbon nanowires for battery applications. *Nano Lett.* **12,** 3783–3787 (2012).
8. Chevrier, V. L. & Ceder, G. Challenges for Na-ion negative electrodes. *J. Electrochem. Soc.* **158,** A1011–A1014 (2011).
9. Abel, P. R. *et al.* Nanocolumnar germanium thin films as a high-rate sodium-ion battery anode material. *J. Phys. Chem. C* **117,** 18885–18890 (2013).

10. Baggetto, L., Keum, J. K., Browning, J. F. & Veith, G. M. Germanium as negative electrode material for sodium-ion batteries. *Electrochem. Commun.* **34,** 41–44 (2013).
11. Zhu, H. *et al.* Tin anode for sodium-ion batteries using natural wood fiber as a mechanical buffer and electrolyte reservoir. *Nano Lett.* **13,** 3093–3100 (2013).
12. Wang, J. W., Liu, X. H., Mao, S. X. & Huang, J. Y. Microstructural evolution of tin nanoparticles during *in situ* sodium insertion and extraction. *Nano Lett.* **12,** 5897–5902 (2012).
13. Jow, T. R., Shacklette, L. W., Maxfield, M. & Vernick, D. The role of conductive polymers in alkali-metal secondary electrodes. *J. Electrochem. Soc.* **134,** 1730–1733 (1987).
14. Darwiche, A. *et al.* Better cycling performances of bulk Sb in Na-ion batteries compared to Li-ion systems: an unexpected electrochemical mechanism. *J. Am. Chem. Soc.* **134,** 20805–20811 (2012).
15. Corbridge, D. E. C. *Phosphorus Chemistry, Biochemistry and Technology* 6th edn (CRC Press, 2013).
16. Cotton, A., Wilkinson, G., Murillo, C. A. & Bochmann, M. *Advanced Inorganic Chemistry* (Wiley, 1999).
17. Qian, J., Qiao, D., Ai, X., Cao, Y. & Yang, H. Reversible 3-Li storage reactions of amorphous phosphorus as high capacity and cycling-stable anodes for Li-ion batteries. *Chem. Commun.* **48,** 8931–8933 (2012).
18. Wang, L. *et al.* Nano-structured phosphorus composite as high-capacity anode materials for lithium batteries. *Angew. Chem. Int. Ed.* **51,** 9034–9037 (2012).
19. Marino, C., Debenedetti, A., Fraisse, B., Favier, F. & Monconduit, L. Activated-phosphorus as new electrode material for Li-ion batteries. *Electrochem. Commun.* **13,** 346–349 (2011).
20. Li, W.-J., Chou, S.-L., Wang, J.-Z., Liu, H.-K. & Dou, S.-X. Simply mixed commercial red phosphorus and carbon nanotube composite with exceptionally reversible sodium-ion storage. *Nano Lett.* **13,** 5480–5484 (2013).
21. Qian, J., Wu, X., Cao, Y., Ai, X. & Yang, H. High capacity and rate capability of amorphous phosphorus for sodium ion batteries. *Angew. Chem. Int. Ed.* **125,** 4731–4734 (2013).
22. Kim, Y. *et al.* An amorphous red phosphorus/carbon composite as a promising anode material for sodium ion batteries. *Adv. Mater.* **25,** 3045–3049 (2013).
23. Yabuuchi, N. *et al.* Phosphorus electrodes in sodium cells: small volume expansion by sodiation and the surface-stabilization mechanism in aprotic solvent. *ChemElectroChem* **1,** 580–589 (2014).
24. Morita, A. Semiconducting black phosphorus. *Appl. Phys. A* **39,** 227–242 (1986).
25. Hultgren, R., Gingrich, N. S. & Warren, B. E. The atomic distribution in red and black phosphorus and the crystal structure of black phosphorus. *J. Chem. Phys.* **3,** 351–355 (1935).
26. Nagao, M., Hayashi, A. & Tatsumisago, M. All-solid-state lithium secondary batteries with high capacity using black phosphorus negative electrode. *J. Power Sources* **196,** 6902–6905 (2011).
27. Park, C.-M. & Sohn, H.-J. Black phosphorus and its composite for lithium rechargeable batteries. *Adv. Mater.* **19,** 2465–2468 (2007).
28. Sun, L.-Q. *et al.* Electrochemical activity of black phosphorus as an anode material for lithium-ion batteries. *J. Phys. Chem. C* **116,** 14772–14779 (2012).
29. Sun, J. *et al.* Formation of stable phosphorus–carbon bond for enhanced performance in black phosphorus nanoparticle–graphite composite battery anodes. *Nano Lett.* **14,** 4573–4580 (2014).
30. Ramireddy, T. *et al.* Phosphorus–carbon nanocomposite anodes for lithium-ion and sodium-ion batteries. *J. Mater. Chem. A* **3,** 5572–5584 (2015).
31. Yazami, R. & Universitaire, D. A reversible graphite–lithium electrochemical generators. *J. Power Sources* **9,** 365–371 (1983).
32. Wu, H. *et al.* Stable cycling of double-walled silicon nanotube battery anodes through solid-electrolyte interphase control. *Nature Nanotech.* **7,** 310–315 (2012).
33. Liu, N. *et al.* A pomegranate-inspired nanoscale design for large-volume-change lithium battery anodes. *Nature Nanotech.* **9,** 187–192 (2014).
34. Li, W. *et al.* High-performance hollow sulfur nanostructured battery cathode through a scalable, room temperature, one-step, bottom-up approach. *Proc. Natl Acad. Sci. USA* **110,** 7148–7153 (2013).
35. Ye, P. D. *et al.* Phosphorene: an unexplored 2D semiconductor with a high hole mobility. *ACS Nano* **8,** 4033–4041 (2014).
36. Reich, E. S. Phosphorene excites materials scientists. *Nature* **506,** 19 (2014).
37. Churchill, H. O. H. & Jarillo-Herrero, P. Two-dimensional crystals: phosphorus joins the family. *Nature Nanotech.* **9,** 330–331 (2014).
38. Li, L. *et al.* Black phosphorus field-effect transistors. *Nature Nanotech.* **9,** 372–377 (2014).
39. Mohiuddin, T. *et al.* Uniaxial strain in graphene by Raman spectroscopy: G peak splitting, Grüneisen parameters, and sample orientation. *Phys. Rev. B* **79,** 205433 (2009).
40. Ferrari, A. C. *et al.* Raman spectrum of graphene and graphene layers. *Phys. Rev. Lett.* **97,** 187401 (2006).
41. Brent, J. R. *et al.* Production of few-layer phosphorene by liquid exfoliation of black phosphorus. *Chem. Commun.* **50,** 13338–13341 (2014).
42. Hernandez, Y. *et al.* High-yield production of graphene by liquid-phase exfoliation of graphite. *Nature Nanotech.* **3,** 563–568 (2008).
43. Sugai, S. Raman and infrared reflection spectroscopy in black phosphorus. *Solid State Commun.* **53,** 753–755 (1985).
44. Vanderborgh, C. A. & Schiferl, D. Raman studies of black phosphorus from 0.25 to 7.7 GPa at 15 K. *Phys. Rev. B* **40,** 9595–9599 (1989).
45. Akahama, Y., Kobayashi, M. & Kawamura, H. Raman study of black phosphorus up to 13 GPa. *Solid State Commun.* **104,** 311–315 (1997).
46. Lu, W. *et al.* Plasma-assisted fabrication of monolayer phosphorene and its Raman characterization. *Nano Res.* **7,** 853–859 (2014).

Acknowledgements

This work was supported by the Department of Energy, Office of Basic Energy Sciences, Division of Materials Sciences and Engineering, under contract DE-AC02-76SF00515. H.W.L. acknowledges support from the Basic Science Research Program through the National Research Foundation of Korea (NRF) funded by the Ministry of Education, Science and Technology under NRF-2012R1A6A3A03038593.

Author contributions

Y.C. and J.S. conceived and designed the experiments. J.S. performed sample fabrication, characterization and electrochemical measurements. H.W.L. participated in part of the experiments and conducted *in situ* TEM and HR-TEM characterization. J.S., M.P., H.W.L. and Y.C. co-wrote the paper. All authors discussed the results and commented on the manuscript. J.S. and H.W.L. contributed equally to this work.

Additional information

Supplementary information is available in the online version of the paper. Reprints and permissions information is available online at www.nature.com/reprints. Correspondence and requests for materials should be addressed to Y.C.

Competing financial interests

The authors declare no competing financial interests.

Methods

Phosphorene and graphene synthesis. Both phosphorene and graphene were prepared by a liquid-phase exfoliation method adapted from the procedure reported previously[41,42]. Black phosphorus was dispersed in NMP (cylindrical vial, 20 ml NMP) at a concentration of 0.1 mg ml^{-1} and sonicated in a sonic bath (Branson 5210 Ultrasonic) for 10 h. Graphite was also dispersed in NMP (20 ml NMP) at a concentration of 0.1 mg ml^{-1} and sonicated in a sonic bath for 30 min. The resultant dispersion of graphene was centrifuged using a Fisher Scientific accuSpin 400 centrifuge for 60 min at 500 r.p.m. to remove sediment and obtain the supernatant, while the resultant dispersion of phosphorene was centrifuged at 5,000 r.p.m. for 30 min. After centrifuging, decantation was carried out by pipetting off the top half of the dispersion. These methods resulted in phosphorene and graphene yields (mass of phosphorene or graphene/starting material mass) of 17 and 3 wt%, respectively. The sediments of black phosphorus and graphite could be reused to produce phosphorene and graphene by repeating the above processes.

Phosphorene–graphene synthesis. Dispersions of phosphorene and graphene were mixed evenly in different volume ratios by stirring, to achieve different carbon/phosphorus molar ratios (Supplementary Table 2). Because phosphorene is oxidized slowly in air, the sandwiched phosphorene–graphene was produced via self-assembly by evaporating the dispersion at 120 °C in a vacuum oven or an argon-filled glove box. The sample was washed with anhydrous ethyl alcohol several times to remove residual NMP, and then heated at 80 °C to evaporate ethyl alcohol to obtain a powder.

Electrochemical characterization. Battery performance was evaluated by galvanostatic cycling of coin (CR 2032) cells with the phosphorene–graphene composite as the working electrode and sodium foil as the counter/reference electrode. The working electrodes were made using a typical slurry method with phosphorene–graphene powders and polyvinylidene fluoride (PVDF) binder with a mass ratio of 9:1 in *N*-methyl-pyrrolidone (NMP) solvent. The mass loading of active material (phosphorene) was ~0.5 mg cm^{-2}, corresponding to a total mass loading of ~1.15 mg cm^{-2}. The thickness of the electrode without a current collector was 6.5 ± 0.3 μm. The electrolyte consisted of 1.0 mol l^{-1} $NaPF_6$ in an ethylene carbonate (EC)–diethyl carbonate (DEC) solution to which was added 10% fluoroethylene carbonate (FEC), which effectively forms stable SEI layers for sodium-ion batteries. Electrochemical data were collected using an Arbin MSTAT battery test system within the potential range 0.02–1.5 V (versus Na/Na^+) at various current densities. The specific capacity was calculated based on the weight of phosphorus. The mass loading of active material was increased to 2 mg cm^{-2} for further study of its performance. The thickness of the electrode without a current collector was 23.8 ± 0.4 μm. The rate and cycling performance are presented in Supplementary Fig. 12.